

Anisotropic Babinet-Invertible Metasurfaces to Realize Transmission-Reflection Switching for Orthogonal Polarizations of Light

Yosuke Nakata,^{1,*} Yoshiro Urade,² Kunio Okimura,³ Toshihiro Nakanishi,² Fumiaki Miyamaru,^{1,4} Mitsuo Wada Takeda,⁴ and Masao Kitano²

¹*Center for Energy and Environmental Science, Shinshu University,
4-17-1 Wakasato, Nagano 380-8553, Japan*

²*Department of Electronic Science and Engineering, Kyoto University, Kyoto 615-8510, Japan*

³*School of Engineering, Tokai University, 4-1-1 Kitakaname, Hiratsuka, Kanagawa 259-1292, Japan*

⁴*Department of Physics, Faculty of Science, Shinshu University,
3-1-1 Asahi, Matsumoto, Nagano 390-8621, Japan*

(Received 19 July 2016; revised manuscript received 21 September 2016; published 28 October 2016)

The electromagnetic properties of an extremely thin metallic checkerboard drastically change from resonant reflection (transmission) to resonant transmission (reflection) when the local electrical conductivity at the interconnection points of the checkerboard is switched. To date, such critical transitions of metasurfaces have been applied only when they have fourfold rotational symmetry, and their application to polarization control, which requires anisotropy, has been unexplored. To overcome this applicability limitation and open up alternative pathways for dynamic deep-subwavelength polarization control by utilizing critical transitions of checkerboardlike metasurfaces, we introduce a universal class of anisotropic Babinet-invertible metasurfaces enabling transmission-reflection switching for each orthogonally polarized wave. As an application of anisotropic Babinet-invertible metasurfaces, we experimentally realize a reconfigurable terahertz polarizer whose transmitting axis can be dynamically rotated by 90°.

DOI: 10.1103/PhysRevApplied.6.044022

I. INTRODUCTION

Metamaterials, which are artificial materials composed of engineered structures, exhibit exotic functionality not readily observed in nature [1]. Two-dimensional metamaterials with thicknesses much thinner than the wavelength of a target light are called metasurfaces [2]. The careful design of metasurfaces enables us to control both the amplitude and the phase of electromagnetic waves [3,4]. Owing to the scale invariance of Maxwell equations, the extraordinary properties of electromagnetic metamaterials and metasurfaces can be theoretically realized for all frequency ranges by altering the size of the structures. In the terahertz frequency range, metamaterials and metasurfaces are considered promising candidates for manipulating terahertz waves because conventional electronics and photonics technologies cannot be directly applied. Various passive and active devices based on metamaterials and metasurfaces have been demonstrated in the terahertz frequency range [5].

When designing metasurfaces in a vacuum, Babinet's principle is often utilized. Babinet's principle relates the scattering fields of a metasurface to a complementary metasurface. The complementary metasurface is obtained by applying a structural inversion to interchange the holes and metallic portions of the given one-layer metallic metasurface [6]. For a more general case, consider a metasurface at $z = 0$ with a spatially varying sheet

impedance of $Z_s(x, y)$, which relates the tangential component (namely, the xy component) of the electric field at (x, y) on $z = 0$ and the surface current density at the same point [7]. The complementary surface with sheet impedance $Z_s^{(\text{comp})}(x, y)$ is obtained by applying an impedance inversion defined as $Z_s^{(\text{comp})}(x, y) = Z_0^2/[4Z_s(x, y)]$, where $Z_0 \approx 377 \Omega$ is the impedance of the vacuum [8].

When considering Babinet's principle, the metallic checkerboard is a special system: the disconnected [off state, Fig. 1(a)] and connected [on state, Fig. 1(b)] checkerboards are complementary with each other [9]. Their electromagnetic-scattering properties drastically change when the connectivity of the checkerboard is altered. Such a critical behavior of checkerboard metasurfaces has been theoretically investigated from the perspective of percolation theory [10] and has been experimentally observed in the microwave [11] and terahertz frequency ranges [9,12]. The checkerboard metasurface has also been characterized in the optical region [13]. The critical property of checkerboard metasurfaces has been applied to reconfigurable transmission lines [14,15], and the critical behavior caused by rotational disorder has also recently been investigated [16].

To control the criticality of the checkerboard, resistive sheets with sheet impedance Z_c can be introduced at the interconnection points of the checkerboard, as shown in Fig. 1(c) [17–19]. The reconfigurable checkerboard is a checkerboard metasurface with a dynamically controllable Z_c . If a metasurface is dynamically switchable to the

*y_nakata@shinshu-u.ac.jp

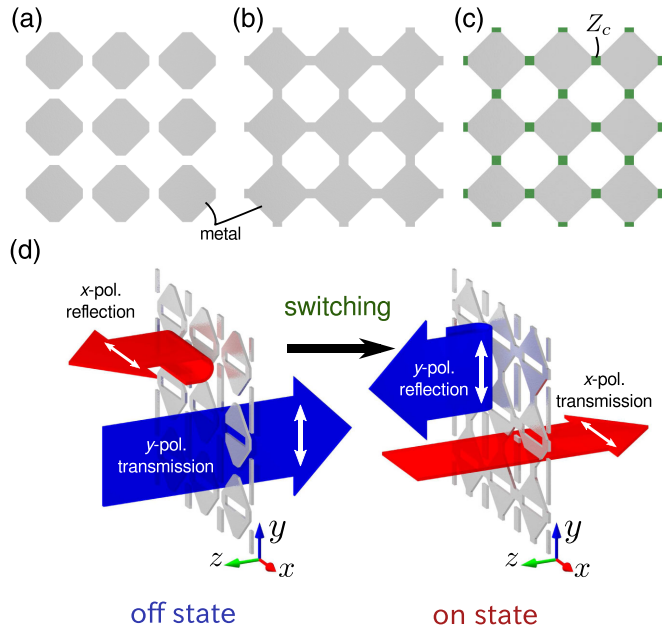


FIG. 1. (a) Off-state checkerboard metasurface. (b) On-state checkerboard metasurface. (c) Babinet-invertible checkerboard metasurface with variable-resistance sheet with sheet impedance Z_c . (d) Dynamic rotation of the transmitting axis of reconfigurable polarizer. The anisotropic checkerboard can be utilized to realize this functionality.

metasurface congruent to the complement of the original, like the reconfigurable checkerboard, it is called *Babinet invertible*. Babinet-invertible metasurfaces are considered to be a generalization of the reconfigurable checkerboard. The fourfold rotational symmetry of the reconfigurable checkerboard and Babinet's principle lead to the relation

$$\tilde{t}_i^{(\text{off})}(\omega) + \tilde{t}_i^{(\text{on})}(\omega) = 1, \quad (1)$$

where the (zeroth-order) complex amplitude transmission coefficients of a normally incident plane wave with an angular frequency ω are denoted by $\tilde{t}_i^{(\text{off})}(\omega)$ and $\tilde{t}_i^{(\text{on})}(\omega)$ for the off-state ($Z_c = \infty$) and on-state ($Z_c = 0$) metasurfaces, respectively [20]. Then the complementary switching of the reconfigurable checkerboard realizes *transmission inversion*, represented by Eq. (1). The transmission inversion of the reconfigurable checkerboard has been applied to a reconfigurable capacitive-inductive terahertz filter [21].

In previous studies of Babinet-invertible metasurfaces, fourfold symmetry is assumed and the polarization dependence of the electromagnetic properties vanishes for normal incidence. Thus, the possibility of dynamic polarization control, which is essential for polarization-sensitive spectroscopy [22,23], through complementary switching has not been explored. In this paper, the applicability limitation of the critical transition of checkerboard metasurfaces to dynamic deep-subwavelength polarization control is overcome by introducing a universal class of anisotropic

Babinet-invertible metasurfaces enabling transmission inversions for each orthogonally polarized wave. To demonstrate one potential application of the proposed class of metasurfaces, we experimentally realize a reconfigurable terahertz polarizer as an anisotropic Babinet-invertible metasurface.

II. THEORY

If we break the rotational symmetry of Babinet-invertible metasurfaces, the (zeroth-order) complex amplitude transmission coefficients \tilde{t}_x and \tilde{t}_y for x - and y -polarized incident waves must be distinguished. Here, we consider an extension of Eq. (1) to such an anisotropic metasurface, as follows:

$$\tilde{t}_x^{(\text{off})}(\omega) + \tilde{t}_x^{(\text{on})}(\omega) = 1, \quad (2)$$

$$\tilde{t}_y^{(\text{off})}(\omega) + \tilde{t}_y^{(\text{on})}(\omega) = 1. \quad (3)$$

Equations (2) and (3) express transmission inversion separately for the two axes, x and y . We therefore name this inversion *transmission inversion for each orthogonal polarization*, which requires a specific symmetry. Note that transmission inversion for each orthogonal polarization and the electric-field continuation condition $1 + \tilde{r}_i^{(\text{off})}(\omega) = \tilde{t}_i^{(\text{off})}(\omega)$ lead to *transmission-reflection switching for each orthogonal polarization* represented by

$$\tilde{t}_i^{(\text{on})}(\omega) = -\tilde{r}_i^{(\text{off})}(\omega), \quad (4)$$

where $\tilde{r}_i^{(\text{off})}(\omega)$ is a complex amplitude reflection coefficient for an i -polarized normally incident plane wave.

Next, we discuss the sufficient symmetry to realize transmission inversion for each orthogonal polarization. The rigorous-vector version of Babinet's principle is expressed as follows [17]:

$$\tilde{t}_x^{(\text{off})}(\omega) + \tilde{t}_y^{(\text{comp})}(\omega) = 1, \quad (5)$$

$$\tilde{t}_y^{(\text{off})}(\omega) + \tilde{t}_x^{(\text{comp})}(\omega) = 1, \quad (6)$$

where $\tilde{t}_i^{(\text{comp})}(\omega)$ represents the (zeroth-order) complex amplitude transmission coefficient for a normally incident plane wave with i polarization onto the metasurface complementary to the off-state one ($i = x, y$). Note that the polarization is rotated by 90° in the complementary problem compared to the original. Comparing Eqs. (5) and (6) with Eqs. (2) and (3), transmission inversion for each orthogonal polarization requires $\tilde{t}_x^{(\text{on})}(\omega) = \tilde{t}_y^{(\text{comp})}(\omega)$ and $\tilde{t}_y^{(\text{on})}(\omega) = \tilde{t}_x^{(\text{comp})}(\omega)$. These equations are satisfied when the metasurface complementary to the off-state surface is obtained by 90° rotation of the on-state surface.

This symmetry condition is sufficient to realize transmission inversion for each orthogonal polarization.

As an application of transmission inversion for each orthogonal polarization, we consider the design of a polarizer whose transmitting axis can be dynamically rotated by 90° , as shown in Fig. 1(d). Designing such a reconfigurable polarizer with variable-resistance elements requires simultaneous fine-tuning for the on- and off-state metasurfaces. This simultaneous fine-tuning is difficult because the on- and off-state metasurfaces generally depend on each other. However, by utilizing transmission inversion for each orthogonal polarization, the problem can be drastically simplified. If we have an off-state Babinet-invertible metasurface with $\tilde{t}_x^{(\text{off})}(\omega_0) \approx 0$ and $\tilde{t}_y^{(\text{off})}(\omega_0) \approx 1$ at an angular frequency ω_0 , then $\tilde{t}_x^{(\text{on})}(\omega_0) \approx 1$ and $\tilde{t}_y^{(\text{on})}(\omega_0) \approx 0$ are automatically satisfied for the on-state metasurface under transmission inversion for each orthogonal polarization. Then, the transmitting axis of the polarizer can be dynamically rotated by 90° . The problem is reduced to designing the off-state Babinet-invertible metasurface with $\tilde{t}_x^{(\text{off})}(\omega_0) \approx 0$ and $\tilde{t}_y^{(\text{off})}(\omega_0) \approx 1$.

We design the reconfigurable terahertz polarizer by using the finite element method solver (COMSOL Multiphysics). To break the fourfold symmetry of the checkerboard, we nest dipoles with their complementary pairs into the checkerboard so that the sufficient condition to realize transmission inversion for each orthogonal polarization can be satisfied. The design of a dipole-nested Babinet-invertible checkerboard metasurface on $z = 0$ is shown in Fig. 2(a). To simplify the analysis, we assume that all of the metal sections are zero-thickness perfect electric conductors. The calculations are performed in the unit cell and periodic boundary conditions are applied to the sides. The top and bottom boundaries are set as ports with only fundamental modes. The plane wave generated by the top port normally enters a metasurface from $z > 0$ to $z < 0$. The basic parameters are set as $a = 106 \mu\text{m}$ and $u = w = 15 \mu\text{m}$. The dipoles and their complements respond only for y polarization. For x -polarized normally

incident waves, the structure responds like a checkerboard without the dipoles. To realize $\tilde{t}_x^{(\text{off})}(\omega_0) \approx 0$, we set a target angular frequency of $\omega_0 \approx 2\pi \times 2.4 \text{ THz}$ near the resonant frequency of the checkerboard. Tuning the dipole length l to realize $\tilde{t}_y^{(\text{off})}(\omega_0) \approx 1$, we obtain $l = 67 \mu\text{m}$. Figures 2(b) and 2(c) show the calculated power-transmission spectra of off- and on-state dipole-nested checkerboards. We observe a 90° transmitting-axis rotation around $\omega = \omega_0$. Because of the resonance nature at $\omega = \omega_0$, an extremely high extinction ratio is achieved in spite of the deep-subwavelength thickness of the metasurface. We also observe that the power-transmission spectra are accurately inverted with respect to the power transmission $T = 1/2$ under the switching. This phenomenon can be explained by Eq. (4). Owing to the mirror symmetry with respect to the x and y axes for the dipole-nested checkerboard, conversion between x and y polarizations does not occur. Then, the power conservation law gives $|\tilde{t}_i^{(\text{off})}(\omega)|^2 + |\tilde{t}_i^{(\text{on})}(\omega)|^2 = 1$ at the angular frequency $\omega \leq \omega_d = 2\pi c/a \approx 2\pi \times 2.83 \text{ THz}$ without any diffraction to higher-order modes, where c is the speed of light in a vacuum. Using Eq. (4), $|\tilde{t}_i^{(\text{off})}(\omega)|^2 + |\tilde{t}_i^{(\text{on})}(\omega)|^2 = 1$ can be written as $|\tilde{t}_i^{(\text{off})}(\omega)|^2 + |\tilde{t}_i^{(\text{on})}(\omega)|^2 = 1$. Figure 3 shows the charge and surface current density of the on-state dipole-nested checkerboard at 1.45, 1.76, 1.96, and 2.37 THz for y -polarized plane waves normally incident from $z > 0$ to $z < 0$. The field distributions at 1.45 and 2.37 THz correspond to those of the on-state dipole-nested checkerboard *without complementary dipoles* shown in Figs. 6(b) and 6(c) of Appendix A. These distributions are not greatly influenced by the introduction of complementary dipoles. On the other hand, the transmission dip at 1.76 THz and peak at 1.96 THz are caused by a hybridization of the complementary dipole mode and those of the on-state dipole-nested checkerboards without complementary dipoles. Further details of multimode formation in the dipole-nested checkerboard is discussed in Appendix A.

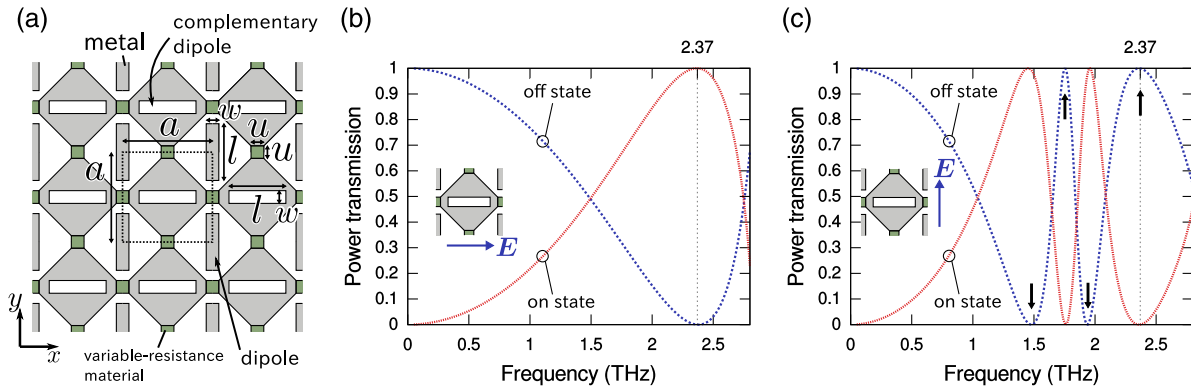


FIG. 2. (a) Design of a dipole-nested Babinet-invertible checkerboard metasurface with $a = 106 \mu\text{m}$, $u = w = 15 \mu\text{m}$, and $l = 67 \mu\text{m}$. Simulated power-transmission spectra of ideal on- and off-state dipole-nested checkerboards at the normal incidence of (b) x - and (c) y -polarized plane waves.

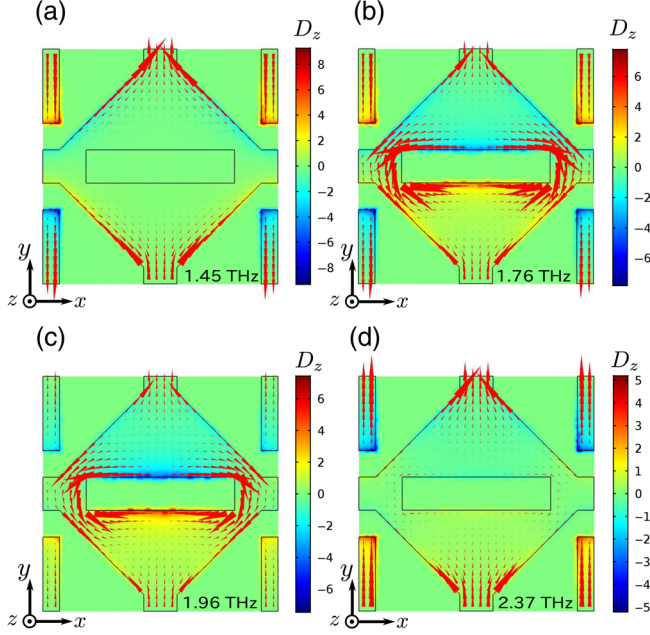


FIG. 3. Electric displacement D_z on the plane $z = a/1000$, corresponding to the surface charge density, and surface current density of the ideal on-state dipole-nested checkerboard at (a) $\omega/(2\pi) = 1.45$ THz, (b) 1.76 THz, (c) 1.96 THz, and (d) 2.37 THz for y -polarized plane waves normally incident from $z > 0$ to $z < 0$. The phase of D_z is shifted by 90° compared to the surface current.

III. EXPERIMENT

Now we consider the experimental demonstration of a reconfigurable dipole-nested checkerboard in the terahertz frequency range. For the variable-resistance sheets, we use vanadium dioxide (VO_2) on a c -cut sapphire substrate. As the temperature increases above $T_c \approx 340$ K, VO_2 exhibits an insulator-to-metal transition where the electrical conductivity typically changes by several orders of magnitude; thus, the metasurface transitions from the off state to the on state. Using the c -cut sapphire as a substrate at $z \leq 0$ causes

mirror symmetry breaking with respect to $z = 0$ where the structures are located, and the condition for Babinet's principle is no longer satisfied. In the target terahertz frequency range, c -cut sapphire has a refractive index $n_x = n_y = n_\perp \approx 3.1$ and $n_z = n_\parallel \approx 3.4$ [24]. To compensate for this substrate effect, we must modify the design of the dipole-nested checkerboard, as shown in Fig. 4(a). In the following discussion, we use the normalized transmission coefficient of the metasurface with a sapphire substrate as $\hat{t}_i = \tilde{t}_i/t_0$ for an i -polarized normally incident wave, where \tilde{t}_i is the amplitude transmission coefficient of the plane $z = 0$ with a metasurface from air to the substrate, and $t_0 = 2/(1 + n_\perp)$ is the Fresnel coefficient for transmission from air to the sapphire. For x -polarized normally incident waves, we change the gap to $g = 5 \mu\text{m}$ to ensure $\hat{t}_x^{(\text{off})}(\omega'_0) \approx 0$ and $\hat{t}_x^{(\text{on})}(\omega'_0) \approx 1$ [21], where ω'_0 is the modified resonant angular frequency. For y -polarized normally incident waves, we use different lengths for the dipoles and their complements. By optimizing these parameters, we obtain $l_1 = 80 \mu\text{m}$ and $l_2 = 69 \mu\text{m}$ to realize $\hat{t}_y^{(\text{off})}(\omega'_0) \approx 1$ and $\hat{t}_y^{(\text{on})}(\omega'_0) \approx 0$. The calculated transmission spectra of the designed metasurface are shown in Fig. 7 of Appendix B.

Next, we experimentally demonstrate dynamic rotation of the transmitting axis of the reconfigurable metasurface. The modified dipole-nested checkerboard is fabricated as follows. A thin film of stoichiometric VO_2 of about $1 \mu\text{m}$ thickness is deposited on a sapphire (0001) substrate (thickness, 1.0 mm) via reactive magnetron sputtering of a vanadium target [25]. After a positive photoresist is patterned on the VO_2 using a maskless lithography technique, the unnecessary part of the VO_2 film is removed by wet etching. The dipole-nested checkerboard made of aluminum (thickness, 400 nm) is formed by photolithography and electron-beam evaporation at room temperature and lift-off techniques. A micrograph of the fabricated sample is shown in Fig. 4(b). The VO_2 squares with target side length

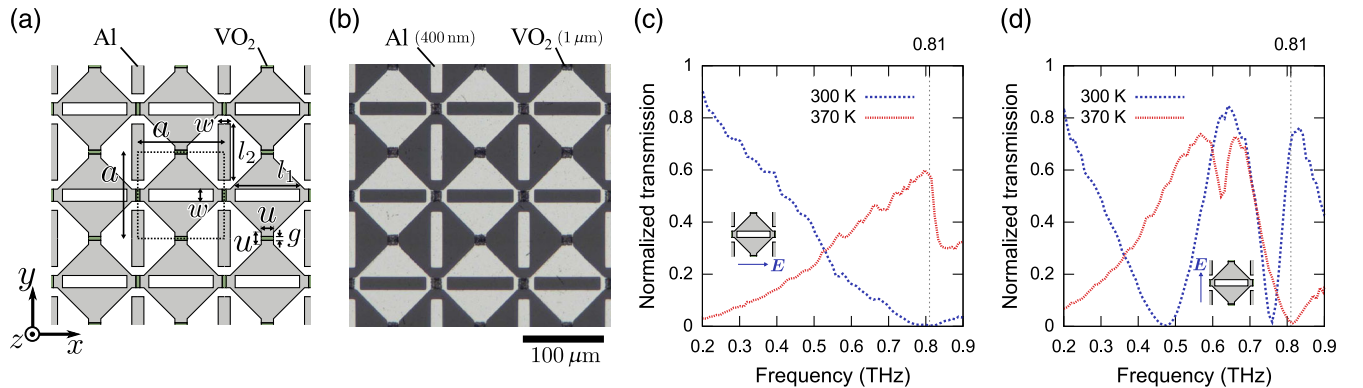


FIG. 4. (a) Design of a dipole-nested checkerboard metasurface on a sapphire substrate. (b) Micrograph of the fabricated dipole-nested checkerboard on a sapphire substrate with the target lengths $a = 106 \mu\text{m}$, $u = w = 15 \mu\text{m}$, $g = 5 \mu\text{m}$, $l_1 = 80 \mu\text{m}$, and $l_2 = 69 \mu\text{m}$. The thicknesses of VO_2 and Al are $1 \mu\text{m}$ and 400 nm , respectively. Normalized power-transmission spectra of the fabricated dipole-nested checkerboard for a normal incidence of a collimated terahertz beam with (c) x and (d) y polarization.

u are partially overlapped by the Al structures, for ensuring electrical connection. The maximum thickness of the device fabricated on a c -cut sapphire substrate is approximately $1.4 \mu\text{m}$, which is deep subwavelength compared to the wavelength at the target frequency.

To evaluate the dipole-nested checkerboard, we use a conventional terahertz time-domain spectroscopy system. To delay the signals reflected at the boundaries, two pieces of c -cut sapphire substrates with a thickness of 1 mm are attached under the metasurface with a 1-mm c -cut sapphire substrate. Therefore, the overall thickness of the substrate is 3 mm. A reference c -cut sapphire sample with a thickness of 3 mm is prepared by stacking three sapphire plates with a thickness of 1 mm. The stacked samples are held by a brass holder with a temperature feedback system to control the electric current in a nichrome wire attached to the holder, while the temperature of the holder is monitored by a thermocouple. A collimated terahertz beam with a linear polarization and beam diameter of approximately 8 mm is normally incident onto the stacked samples. The temporal profile of the electric field is measured using a detector dipole antenna. The multiple reflected signal is cut using a time-domain window function. Measuring the electric fields $E_{\text{ref}}(t)$ of the c -cut reference sapphire substrate and $E(t)$, we calculate the normalized complex amplitude transmission coefficient $\hat{t}(\omega) = \tilde{E}(\omega)/\tilde{E}_{\text{ref}}(\omega)$, where $\tilde{E}(\omega)$ and $\tilde{E}_{\text{ref}}(\omega)$ are Fourier-transformed electric fields. Figures 4(c) and 4(d) show the power-transmission spectra $|\hat{t}|^2$ of the dipole-nested checkerboard on a sapphire substrate for normal incidence of collimated terahertz beams with x and y polarization, respectively. The lowest diffraction frequency of the dipole-nested checkerboard is given by $f_d = c/(n_{\parallel}a) \approx 0.83 \text{ THz}$. At 0.81 THz, the dynamic rotation of the transmitting axis of the metasurface from the y axis to the x axis is realized by heating the device. The extinction ratios $|\hat{t}_y^{(\text{off})}(\omega'_0)/\hat{t}_x^{(\text{off})}(\omega'_0)|^2$ and $|\hat{t}_x^{(\text{on})}(\omega'_0)/\hat{t}_y^{(\text{on})}(\omega'_0)|^2$ at $\omega'_0 = 2\pi \times 0.81 \text{ THz}$ are approximately 10^2 . Although the frequency dependences of the transmission spectra agree well with the simulated data shown in Fig. 7 of Appendix B, the maximum transmission peaks of the on- and off-state metasurfaces are not as high as the simulated data. This result occurs because the resistivity of the VO_2 film is not switched ideally and the aluminum has a finite conductivity. High-quality vanadium-dioxide films formed by other deposition techniques, such as pulse-laser deposition [26], and higher conductive metals could improve the performance of the device.

IV. CONCLUSION

In this paper, we introduce the class of anisotropic Babinet-invertible metasurfaces enabling transmission-reflection switching for each orthogonally polarized wave, and experimentally demonstrate their applicability to polarization control of electromagnetic waves. The

transmission inversion for each orthogonal polarization can be considered a manifestation of an artificially engineered insulator-metal transition of anisotropic metasurfaces. The concept of anisotropic Babinet-invertible metasurfaces enabling transmission-reflection switching for each orthogonally polarized wave is universal, and it is independent of the implementation. Their applications are not limited to reconfigurable terahertz polarizers, but they could find a wide range of applications for dynamic polarization control over a broad region of the electromagnetic spectrum in which the variable-resistance materials can be used. Ultrafast switching can be realized if photoexcitation of carriers is employed. Thus, the anisotropic Babinet-invertible metasurfaces will pave the way for ultrafast polarization-selective spectroscopy.

ACKNOWLEDGMENTS

The authors gratefully acknowledge the contributions of T. Nishida and T. McArthur. The sample fabrication was performed with the help of Kyoto University Nano Technology Hub, as part of the ‘‘Nanotechnology Platform Project,’’ sponsored by MEXT, Japan. The present research is supported by a grant from the Murata Science Foundation and by JSPS KAKENHI Grant No. JP16K13699. Y.U. was supported by a JSPS Research Fellowship for Young Scientists.

APPENDIX A: MULTIMODE FORMATION IN DIPOLE-NESTED CHECKERBOARD

Here, we investigate the formation of the multiple resonances of a dipole-nested checkerboard in a vacuum. The field distributions of on- and off-state metasurfaces are exactly related to each other, so we focus only on the on-state metasurface. We first study the transmission spectra and field distribution of each component of the dipole-nested checkerboard in a vacuum by COMSOL using the parameters for a dipole-nested checkerboard shown in Fig. 2: $a = 106 \mu\text{m}$, $u = w = 15 \mu\text{m}$, and $l = 67 \mu\text{m}$. Periodic boundary conditions are applied at the sides of the unit cell, and the ports with the lowest frequency modes are set on the bottom and top faces. The metallic structures are assumed to be zero-thickness perfect electric conductors. Normally incident y -polarized plane waves enter the metasurface at $z = 0$ from $z > 0$ to $z < 0$. Figure 5(a) shows the transmission spectra of the dipoles and the on-state checkerboard. The dipoles and the on-state checkerboard show a transmission dip at 2.03 THz and a transmission peak at 2.42 THz. The electric displacement D_z just above the surface ($z = a/1000$), corresponding to the charge density, and the surface current distributions on the metal ($z = 0$) at these frequencies are shown in Figs. 5(b) and 5(c). To clearly see the distributions, the phase of D_z is shifted by 90° compared to the surface current in these plots. The first-order resonance of the dipoles is shown in

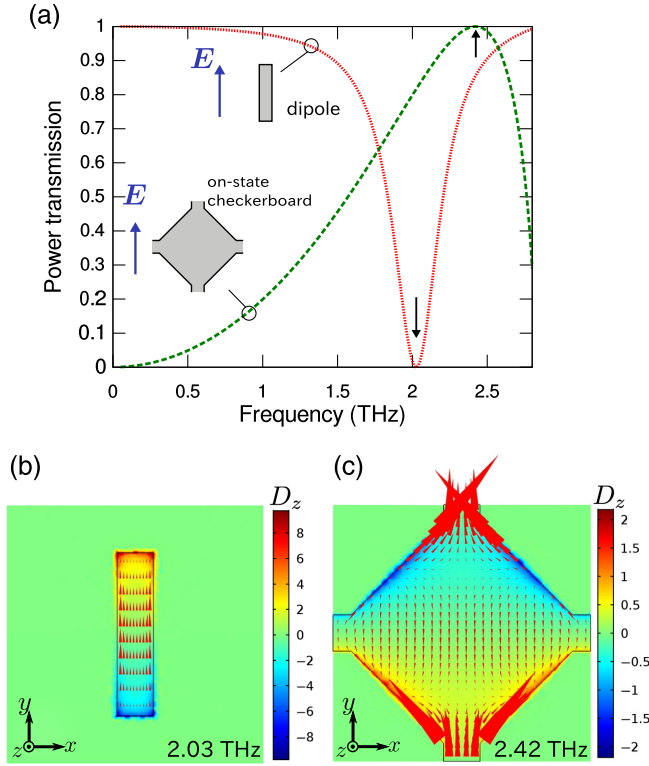


FIG. 5. (a) Transmission spectra of dipoles and the on-state checkerboard with $a = 106 \mu\text{m}$, $u = w = 15 \mu\text{m}$, and $l = 67 \mu\text{m}$. The electric displacement D_z on the plane $z = a/1000$, corresponding to the surface charge density, and surface current density of (b) dipoles at $\omega/(2\pi) = 2.03 \text{ THz}$ and (c) the on-state checkerboard at 2.42 THz . The phase of D_z is shifted by 90° compared to the surface current.

Fig. 5(b). In Fig. 5(c), the direction of the surface current at the center of the on-state checkerboard is the opposite of that on the top and bottom interconnection patches.

Next, we consider the on-state checkerboard combined with dipoles. The spectrum of the on-state checkerboard with dipoles at the normal incidence of y -polarized plane waves is shown in Fig. 6(a). It shows Fano-like characteristics [27] with transmission peaks at 1.45 and 2.72 THz , and a transmission dip at 2.32 THz . The charge and surface current distributions on the dipoles at 1.45 [Fig. 6(b)] and 2.32 THz [Fig. 6(c)] are similar to those shown in Fig. 5(b). At these frequencies, the phase relations between the currents on the checkerboard and the dipole are opposing, and the resonant transmission at 1.45 THz and the reflection at 2.32 THz are caused by interference between the first-order dipole mode and the on-state checkerboard mode. The current distributions on the checkerboard and the dipole at 2.72 THz in Fig. 6(d) are similar to those in Figs. 5(b) and 5(c), respectively. This similarity indicates that the 2.72-THz resonant transmission originates from a hybridized mode of the first-order dipole mode and the 2.42-THz on-state checkerboard mode.

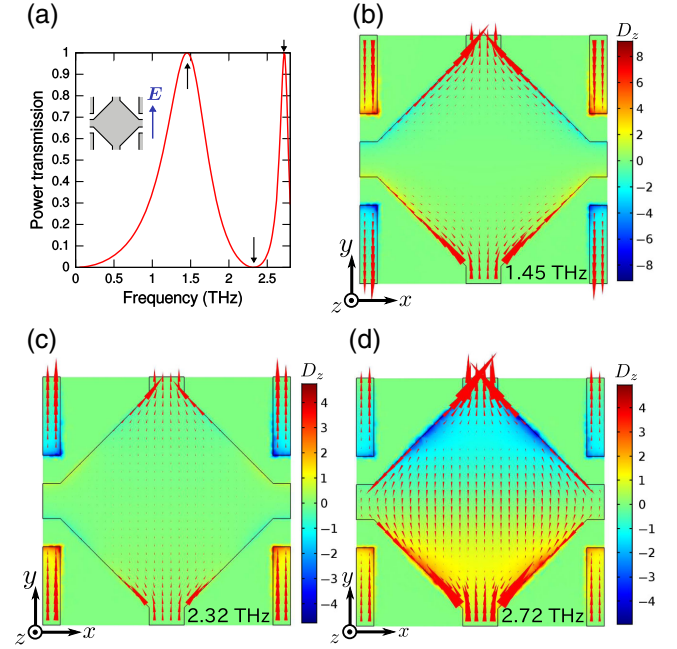


FIG. 6. (a) Transmission spectrum of an on-state checkerboard with dipoles having $a = 106 \mu\text{m}$, $u = w = 15 \mu\text{m}$, and $l = 67 \mu\text{m}$. Electric displacement D_z on the plane $z = a/1000$, corresponding to the surface charge density, and the surface current density on the metasurface at (b) $\omega/(2\pi) = 1.45$, (c) 2.32 , and (d) 2.72 THz . The phase of D_z is shifted by 90° compared to the surface current.

APPENDIX B: SIMULATION FOR MODIFIED DIPOLE-NESTED CHECKERBOARD ON A c -CUT SAPPHIRE SUBSTRATE

Here, we present spectra of a modified dipole-nested checkerboard on a c -cut sapphire substrate. The geometrical parameters are $a = 106 \mu\text{m}$, $u = w = 15 \mu\text{m}$, $g = 5 \mu\text{m}$, $l_1 = 80 \mu\text{m}$, and $l_2 = 69 \mu\text{m}$. We assume that all of the conductive parts are zero-thickness perfect electric conductors. The calculation is performed in the unit cell, and periodic boundary conditions are imposed on the sides.

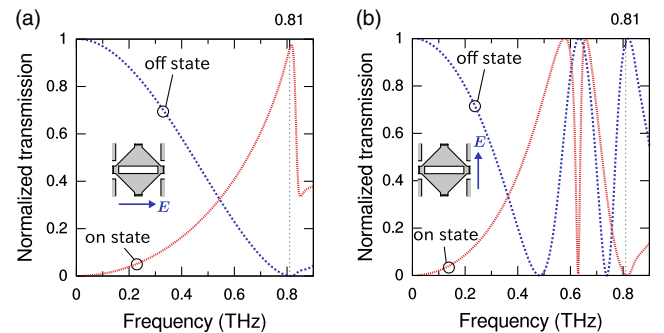


FIG. 7. Calculated normalized power-transmission spectra of a modified dipole-nested checkerboard on a c -cut sapphire substrate at the normal incidence of (a) x - and (b) y -polarized plane waves. The geometrical parameters are $a = 106 \mu\text{m}$, $u = w = 15 \mu\text{m}$, $g = 5 \mu\text{m}$, $l_1 = 80 \mu\text{m}$, and $l_2 = 69 \mu\text{m}$.

The metallic structures are located on $z = 0$. A linearly polarized plane wave is generated from a perfectly-matched-layer-backed port with a slit condition on the interior port, and it is detected by another port with a similar setting. The refractive index of the c -cut sapphire is set to be $n_x = n_y = n_{\perp} = 3.1$ and $n_z = n_{\parallel} = 3.4$. The calculated normalized power-transmission spectra $|\tilde{t}|^2$ are shown in Fig. 7.

- [1] L. Solymar and E. Shamonina, *Waves in Metamaterials* (Oxford University Press, New York, 2009).
- [2] A. V. Kildishev, A. Boltasseva, and V. M. Shalaev, Planar photonics with metasurfaces, *Science* **339**, 1232009 (2013).
- [3] F. Monticone, N. M. Estakhri, and A. Alù, Full Control of Nanoscale Optical Transmission with a Composite Metascreen, *Phys. Rev. Lett.* **110**, 203903 (2013).
- [4] C. Pfeiffer and A. Grbic, Metamaterial Huygens' Surfaces: Tailoring Wave Fronts with Reflectionless Sheets, *Phys. Rev. Lett.* **110**, 197401 (2013).
- [5] H. Tao, W. J. Padilla, X. Zhang, and R. D. Averitt, Recent progress in electromagnetic metamaterial devices for terahertz applications, *IEEE J. Sel. Top. Quantum Electron.* **17**, 92 (2011).
- [6] H. Booker, Slot aerials and their relation to complementary wire aerials (Babinet's principle), *J. Inst. Electr. Eng. Part III A* **93**, 620 (1946).
- [7] Rigorously, the sheet impedance is defined as $\tilde{\mathbf{E}}_{\parallel}(x, y) = Z_s(x, y)\tilde{\mathbf{K}}(x, y)$ for the tangential component of the electric field $\tilde{\mathbf{E}}_{\parallel}(x, y)\exp(-i\omega t) + \text{c.c.}$ on $z = 0$ and surface current density $\tilde{\mathbf{K}}(x, y)\exp(-i\omega t) + \text{c.c.}$ on $z = 0$. Here, ω is an angular frequency and c.c. represents the complex-conjugate operation.
- [8] C. E. Baum and H. N. Kritikos, *Electromagnetic Symmetry* (Taylor and Francis, Washington, 1995).
- [9] R. C. Compton, J. C. Macfarlane, L. B. Whitbourn, M. M. Blanco, and R. C. McPhedran, Babinet's principle applied to ideal beam-splitters for submillimetre waves, *Opt. Acta* **31**, 515 (1984).
- [10] K. Kempa, Percolation effects in the checkerboard Babinet series of metamaterial structures, *Phys. Status Solidi RRL* **4**, 218 (2010).
- [11] J. D. Edmunds, A. P. Hibbins, J. R. Sambles, and I. J. Youngs, Resonantly inverted microwave transmissivity threshold of metal grids, *New J. Phys.* **12**, 063007 (2010).
- [12] K. Takano, F. Miyamaru, K. Akiyama, H. Miyazaki, M. W. Takeda, Y. Abe, Y. Tokuda, H. Ito, and M. Hangyo, Crossover from capacitive to inductive electromagnetic responses in near self-complementary metallic checkerboard patterns, *Opt. Express* **22**, 24787 (2014).
- [13] S. A. Ramakrishna, P. Mandal, K. Jeyadheepan, N. Shukla, S. Chakrabarti, M. Kadac, S. Enoch, and S. Guenneau, Plasmonic interaction of visible light with gold nanoscale checkerboards, *Phys. Rev. B* **84**, 245424 (2011).
- [14] D. González-Ovejero, E. Martini, B. Loiseaux, C. Tripon-Canseliet, M. J. Mencagli, J. Chazelas, and S. Maci, Basic properties of checkerboard metasurfaces, *IEEE Antennas Wireless Propag. Lett.* **14**, 406 (2015).
- [15] D. González-Ovejero, E. Martini, and S. Maci, Surface waves supported by metasurfaces with self-complementary geometries, *IEEE Trans. Antennas Propag.* **63**, 250 (2015).
- [16] B. Tremain, C. J. Durrant, I. E. Carter, A. P. Hibbins, and J. R. Sambles, The effect of rotational disorder on the microwave transmission of checkerboard metal square arrays, *Sci. Rep.* **5**, 16608 (2015).
- [17] Y. Nakata, Y. Urade, T. Nakanishi, and M. Kitano, Plane-wave scattering by self-complementary metasurfaces in terms of electromagnetic duality and Babinet's principle, *Phys. Rev. B* **88**, 205138 (2013).
- [18] Y. Urade, Y. Nakata, T. Nakanishi, and M. Kitano, Frequency-Independent Response of Self-Complementary Checkerboard Screens, *Phys. Rev. Lett.* **114**, 237401 (2015).
- [19] Y. Urade, Y. Nakata, T. Nakanishi, and M. Kitano, Broadband and energy-concentrating terahertz coherent perfect absorber based on a self-complementary metasurface, *Opt. Lett.* **41**, 4472 (2016).
- [20] Note that the complex amplitude transmission coefficient \tilde{t} from an incident wave $\tilde{\mathbf{E}}_0 \exp[i(\mathbf{k}_0 \cdot \mathbf{x} - \omega t)] + \text{c.c.}$ to a transmitted wave $\tilde{\mathbf{E}}_t \exp[i(\mathbf{k}_t \cdot \mathbf{x} - \omega t)] + \text{c.c.}$ is defined by $\tilde{\mathbf{E}}_t = \tilde{t}\tilde{\mathbf{E}}_0$. In this paper, the modifier *zeroth-order* represents the case in which \mathbf{k}_t satisfies $\mathcal{P}\mathbf{k}_t = \mathcal{P}\mathbf{k}_0$, where $\mathcal{P}: (v_x, v_y, v_z)^T \mapsto (v_x, v_y, 0)^T$ is the projection operator onto $z = 0$ (T represents "transpose").
- [21] Y. Urade, Y. Nakata, K. Okimura, T. Nakanishi, F. Miyamaru, M. W. Takeda, and M. Kitano, Dynamically Babinet-invertible metasurface: A capacitive-inductive reconfigurable filter for terahertz waves using vanadium-dioxide metal-insulator transition, *Opt. Express* **24**, 4405 (2016).
- [22] N. C. J. van der Valk, W. A. M. van der Marel, and P. C. M. Planken, Terahertz polarization imaging, *Opt. Lett.* **30**, 2802 (2005).
- [23] S. Katletz, M. Pflieger, H. Pühringer, M. Mikulics, N. Vieweg, O. Peters, B. Scherger, M. Scheller, M. Koch, and K. Wiesauer, Polarization sensitive terahertz imaging: Detection of birefringence and optical axis, *Opt. Express* **20**, 23025 (2012).
- [24] D. Grischkowsky, S. Keiding, M. van Exter, and C. Fattinger, Far-infrared time-domain spectroscopy with terahertz beams of dielectrics and semiconductors, *J. Opt. Soc. Am. B* **7**, 2006 (1990).
- [25] K. Okimura, Y. Sasakawa, and Y. Nihei, X-ray diffraction study of electric field-induced metal-insulator transition of vanadium dioxide film on sapphire substrate, *Jpn. J. Appl. Phys.* **45**, 9200 (2006).
- [26] J. Nag and R. F. Haglund, Jr., Synthesis of vanadium dioxide thin films and nanoparticles, *J. Phys. Condens. Matter* **20**, 264016 (2008).
- [27] A. E. Miroshnichenko, S. Flach, and Y. S. Kivshar, Fano resonances in nanoscale structures, *Rev. Mod. Phys.* **82**, 2257 (2010).